Reduced partition function ratios of iron and oxygen in goethite

Marc Blanchard, N. Dauphas, M.Y. Hu, M. Roskosz, E.E. Alp, D.C. Golden,
C.K. Sio, F.L.H. Tissot, J. Zhao, L. Gao, et al.

HAL Id: hal-01096956

https://hal.sorbonne-universite.fr/hal-01096956v1

Submitted on 18 Dec 2014

2

3   **Reduced partition function ratios of iron and oxygen in goethite**

4

5   M. Blanchard [a,*], N. Dauphas [b], M.Y. Hu [c], M. Roskosz [d], E.E. Alp [c], D.C.

6   Golden [e], C.K. Sio [b], F.L.H. Tissot [b], J. Zhao [c], L. Gao [c], R.V. Morris [f], M.

7   Fornace [b], A. Floris [g], M. Lazzeri [a], E. Balan [a]

8

9   [a] Institut de Minéralogie, de Physique des Matériaux, et de Cosmochimie (IMPMC),
10   Sorbonne Universités - UPMC Univ Paris 06, UMR CNRS 7590, Muséum National
11   d'Histoire Naturelle, IRD UMR 206, 4 Place Jussieu, F-75005 Paris, France.
12   [b] Origins Laboratory, Department of the Geophysical Sciences and Enrico Fermi
13   Institute, The University of Chicago, 5734 South Ellis Avenue, Chicago, IL 60637,
14   USA
15   [c] Advanced Photon Source, Argonne National Laboratory, 9700 South Cass Avenue,
16   Argonne, IL 60439, USA
17   [d] Unité Matériaux et Transformations, Université Lille 1, CNRS UMR 8207, 59655
18   Villeneuve d'Ascq, France
19   [e] Engineering and Science Contract Group-Hamilton Sundstrand, Mail Code JE23,
20   Houston, TX 77058, USA
21   [f] NASA Johnson Space Center, Houston, TX, USA
22   [g] Department of Physics, King's College London, London, Strand WC2R 2LS, United
23   Kingdom
24
25
26   Corresponding Author: Marc Blanchard (marc.blanchard@impmc.upmc.fr)

27   Tel.: +33 1 44 27 98 22   Fax: +33 1 44 27 37 85

28

28   **Abstract**

29

30   First-principles calculations based on the density functional theory (DFT) with

31   or without the addition of a Hubbard U correction, are performed on goethite in order

32   to determine the iron and oxygen reduced partition function ratios (β-factors). The

33   calculated iron phonon density of states (pDOS), force constant and β-factor are

34   compared with reevaluated experimental β-factors obtained from Nuclear Resonant

35   Inelastic X-ray Scattering (NRIXS) measurements. The reappraisal of old

36   experimental data is motivated by the erroneous previous interpretation of the low-

37   and high-energy ends of the NRIXS spectrum of goethite and jarosite samples

38   (Dauphas et al. 2012). Here the NRIXS data are analyzed using the SciPhon software

39   that corrects for non-constant baseline. New NRIXS measurements also demonstrate

40   the reproducibility of the results. Unlike for hematite and pyrite, a significant

41   discrepancy remains between DFT, NRIXS and the existing Mössbauer-derived data.

42   Calculations suggest a slight overestimation of the NRIXS signal possibly related to

43   the baseline definition. The intrinsic features of the samples studied by NRIXS and

44   Mössbauer spectroscopy may also contribute to the discrepancy (*e.g.* internal

45   structural and/or chemical defects, microstructure, surface contribution). As for

46   oxygen, DFT results indicate that goethite and hematite have similar β-factors, which

47   suggests almost no fractionation between the two minerals at equilibrium.

48

49

1. INTRODUCTION

50   For decades now, the isotopic compositions of natural samples have been

51   measured and found countless applications in all branches of geosciences (see for

52   reviews, Valley and Cole, 2001; Johnson et al. 2004; Eiler et al. 2014). In the

53   meantime, isotope exchange experiments were performed to improve our

54   understanding of the processes responsible for stable isotope fractionation. More

55   recently, new approaches have emerged and are contributing to this field of research.

56   First-principles calculations give reduced partition function ratios (also called β-

57   factors) that can be combined for two phases in order to obtain the equilibrium isotope

58   fractionation factor (α-factor), which is the quantity usually measured. These

59   theoretical methods are also of great interest for investigating the mechanisms

60   controlling the isotope fractionation at the molecular scale. For Mössbauer active

61   elements (like iron), β-factors can also be obtained using Mössbauer spectroscopy

62   through the measurement of the temperature dependence of the isomer shift

63   (Polyakov and Mineev, 2000) or using Nuclear Resonant Inelastic X-ray Scattering

64   (NRIXS, Polyakov et al., 2005, 2007; Dauphas et al., 2012, 2014).

65   Dauphas et al. (2012) and Hu et al. (2013) reported NRIXS data for ^{57}Fe-rich

66   goethite FeO(OH), hydronium-jarosite $(H_3O)Fe_3(SO_4)_2(OH)_6$ and potassium jarosite

67     $KFe_3(SO_4)_2(OH)_6$. From such measurements, one can deduce iron β-factors as a

68   function of temperature. Polyakov et al. (2007) had used projected partial phonon

69   density of states (pDOS) obtained using this technique to calculate β-factors for

70   various phases. Dauphas et al. (2012) and Hu et al. (2013) used a different approach

71   based on moment estimates of NRIXS scattering spectrum S(E), which simplifies

72   evaluation of measurement uncertainties and potential systematic errors. The study of

73   Dauphas et al. (2012) was the first of its kind in measuring NRIXS spectra

74   specifically for applications to isotope geochemistry. In doing so, they encountered a

75   difficulty that had been unappreciated before concerning the baseline at low and high

76   energies. Most previous studies in geosciences had focused on estimating the Debye

77   sound velocity (Hu et al. 2003; Sturhahn and Jackson, 2007), from which

78   compressional and shear wave velocities can be deduced if the bulk modulus and

79   density of the phase are known. These estimates are derived from parts of the spectra

80   that are close to the elastic peak for the nuclear transition of ^{57}Fe at 14.4125 keV. On

81   the other hand, the force constant, which controls β-factors, is heavily influenced by

82   details of the spectrum at the low- and high-energy ends of the spectrum. As a result,

83   little attention had been paid to the accuracy of force constant measurements by

84   NRIXS. Dauphas et al. (2012) found that in some cases, significant counts were

85   present even at high energies. The projected partial phonon density of states, g(E), and

86   the scattering spectrum, S(E), never reached zero and as a result, the integrals that

87   gave the force constants did not plateau for goethite and H-jarosite. These were

88   interpreted to reflect the presence of multiple phonons at high energies. However, we

89   were unable to replicate the measurements during another session of NRIXS

90   measurements at the Advanced Photon Source synchrotron. This and other tests

91   performed on other phases convinced us that the high counts in the tails are not from

92   multiple phonons but rather reflect the presence of a non-constant baseline. To

93   address this issue, Dauphas and collaborators have developed a software (SciPhon)

94   that reliably corrects for non-constant baseline (Dauphas et al, 2014).

95   In the present study, the pDOS as well as the iron and oxygen β-factors of

96   goethite are computed using first-principles calculations and compared to available

97   experimental isotopic data. In parallel, the data published in Dauphas et al. (2012)

98   have been re-evaluated using SciPhon and we present revised estimates for the force

99   constants of goethite and jarosite. To validate the approach and evaluate the long-term

100   reproducibility of force constant measurements by NRIXS, we have analyzed the

101   goethite sample two more times and the jarosite samples one more time. Those new

102   results, together with a re-evaluation of previous data, are reported here.

103

104   **2. MATERIALS AND METHODS**

105   **2.1. NRIXS spectroscopy**

106   Nuclear resonant inelastic X-ray scattering is a nuclear spectroscopic

107   technique that uses the nuclear transition of ^{57}Fe at 14.4125 keV to probe the vibration

108   properties of iron (Seto et al. 1995; Sturhahn et al. 1995). The method as implemented

109   at sector 3-ID-B of the Advanced Photon Source at Argonne National Laboratory is

110   briefly described hereafter. The incident beam is a pulsed X-ray beam of 70 ps

111   duration and 153 ns interpulse duration. A monochromator restricts the energy spread

112   of the incident beam to 1 meV. When the pulse hits the sample, X-rays are scattered

113   by electrons and this electronic contribution is almost instantaneous. On the other

114   hand, the excited ^{57}Fe nuclei have a finite lifetime of 141 ns and the electronic

115   contribution can be eliminated from the signal by applying some time discrimination.

116   The signal from NRIXS is measured using Avalanche Photodiodes (APD). The

117   energy is scanned around the nominal resonant energy over a typical interval of -150

118   to +150 meV. When the photon energy is higher than the resonance energy, the

119   excess energy can be lost to excitation of phonon modes in the lattice and the nuclear

120   excitation can still occur (phonon creation). When the energy is lower than the

121   nominal resonance energy, the energy deficit can be provided by lattice vibrations and

122   the nuclear excitation can still occur (phonon annihilation).

123   From NRIXS spectra one can calculate β-factors by taking the moments of the

124   scattering spectrum S(E) (Dauphas et al. 2012; Hu et al. 2013) or the projected partial

125   phonon density of states g(E) (Polyakov et al. 2005, Dauphas et al. 2012). In the

126   present study, all samples were fine powders (isotropic) and the calculated pDOS

127   represents an average from contributions of all crystallographic orientations. The

128   pDOS is partial in the sense that NRIXS is only sensitive to ^{57}Fe. Using S(E), the

129   formula that gives β-factors is (Dauphas et al. 2012),

130    $$1000 \ln \beta \approx 1000 \left(\frac{M}{M^*} - 1 \right) \frac{1}{E_R} \left[\frac{R_3^S}{8k^2T^2} - \frac{R_5^S - 10R_2^S R_3^S}{480k^4T^4} + \frac{R_7^S + 210\left(R_2^S\right)^2 R_3^S - 35R_3^S R_4^S - 21R_2^S R_5^S}{20160k^6T^6} \right]$$

131   , (Eq. 1)

132   where M and M^* are the masses of the two isotopes considered (*e.g.*, 56 and 54), E_R is

133   the free recoil energy (1.956 meV for ^{57}Fe), k is Boltzmann's constant, T is the

134   temperature, and R_i^S is the ith centered moment of S given by

135    $R_i^S = \int_{-\infty}^{+\infty} S(E)(E - E_R)^i dE$. Equation (1) was derived by Dauphas et al. (2012) and

136   Hu et al. (2013) using two different mathematical approaches (expansions in powers

137   of temperature *vs.* thermalized moments).

138   The β-factors can also be calculated from g(E) using the formula that is valid for E/kT

139    $< 2\pi$ (Polyakov et al. 2005, Dauphas et al. 2012),

140    $$1000 \ln \beta \approx 1000 \left(\frac{M}{M^*} - 1 \right) \left[\frac{m_2^g}{8k^2T^2} - \frac{m_4^g}{480k^4T^4} + \frac{m_6^g}{20160k^6T^6} \right], \qquad \text{(Eq. 2)}$$

141   where m_i^g is the ith moment of g given by $m_i^g = \int_0^{+\infty} g(E)E^i dE$. Polyakov et al. (2005)

142   obtained this formula using perturbation theory and an expression of the kinetic

143   energy while Dauphas et al. (2012) obtained this formula using a Bernoulli expansion

144   of the reduced partition function ratio. In general, β-factors can be expressed as,

145
$$1000 \ln \beta = \frac{A_1}{T^2} + \frac{A_2}{T^4} + \frac{A_3}{T^6},$$
(Eq. 3)

146 where the coefficients A_1, A_2, and A_3 can be calculated from either Eq. 1 (S) or Eq. 2

147 (g). The pDOS g is calculated from S using a Fourier-Log decomposition (Johnson

148 and Spence, 1974; Sturhahn et al. 1995; Sturhahn 2000; Kohn and Chumakov 2000)

149 and Eqs. 1 and 2 are mathematically equivalent. In practice, Eq. 1 is easier to use as

150 errors are not correlated between different energy channels and it is more

151 straightforward to assess the effects of the data reduction procedure (*e.g.*, truncation

152 in energy, baseline subtraction) on the estimates of the β-factor coefficients. The

153 above-mentioned equations can also be written as (Dauphas et al. 2012),

154
$$1000 \ln \beta = \frac{B_1 \langle F \rangle}{T^2} - \frac{B_2 \langle F \rangle^2}{T^4},$$
(Eq. 4)

155 where $B_1 = 2853$, B_2 is a constant that depends on the shape of the pDOS and $\langle F \rangle$ is

156 the mean force constant (in N/m) of the bonds holding iron in position,

157
$$\langle F \rangle = \frac{M}{E_R \hbar^2} R_3^S = \frac{M}{\hbar^2} m_2^g.$$
(Eq. 5)

158 The same samples as those initially measured by Dauphas et al. (2012) were used in

159 this study and details on the synthesis method can be found in Golden et al. (2008).

160 All samples were made starting with ^{57}Fe-rich metal (95 % *vs* 2.1 % natural

161 abundance) as NRIXS is only sensitive to this Mössbauer isotope. The nature of the

162 minerals analyzed was checked by X-ray powder diffraction (XRD). The Rietveld

163 refinement (JADE software package, Materials Data Inc.) provided the following

164 unit-cell parameters for the goethite sample: $a = 4.58$ Å, $b = 9.94$ Å, $c = 3.02$ Å

165 (*Pbnm* space group). The particle sizes (equivalent sphere diameters of coherent

166 domain sizes) were determined using the peak broadening of Rietveld-refined XRD,

167 yielding 19.8 nm for goethite and 223.0 nm for K-Jarosite. Goethite particles are

168 usually acicular. In Dauphas et al 2012, the powdered samples were mounted in

169 compressed pellets, which could impart preferential orientation of the samples, as

170 rightly noticed by Frierdich et al. (2014). However, the latter measurements were

171 done on the powdered samples mounted in vacuum grease at the tip of a kapton

172 capillary, which should keep a random orientation of the particles. One or two APDs

173 were mounted on the sides of the sample perpendicular to the incident beam, so as to

174 capture the maximum solid angle of scattered X-rays. The forward signal was

175 measured at the same time, providing an accurate estimate of the resolution function.

176 The data reduction was entirely done using a new software called SciPhon that

177 is introduced briefly in Dauphas et al. (2014) and will be the scope of a forthcoming

178 publication. The main difference with the data reduction protocol used by Dauphas et

179 al. (2012) is the recognition that signal is present at the low and high energy ends of

180 the spectrum at a level that is too high to be explained by the presence of multiple

181 phonons. The approach used in SciPhon is to remove a linear baseline that is

182 calculated by interpolating the data between the low and high-energy ends of the

183 spectrum and truncating the data when the signal reaches a constant value. This is an

184 effective method when a broad enough energy scan is acquired and one can clearly

185 make the cut between what is signal and what is baseline. After truncation and

186 baseline subtraction, the missing signal is reconstructed by calculating the

187 contribution from the missing multiple phonons using a first estimate of g obtained

188 from truncated S. When the baseline at the high-energy end is higher than at the low-

189 energy end (most common situation), the correction for non-constant baseline brings

190 the force constant down. Conversely, when the baseline at the high-energy end is

191 lower than at the high-energy end, the correction brings the force constant up. The

192 other features of SciPhon are deconvolution of the resolution function using a steepest

193   descent algorithm, removal of the elastic peak using a refined interpolation method,

194   calculation of all parameters needed for application of NRIXS data to isotope

195   geochemistry (Eqs. 1 and 2), and propagation of all uncertainties (not only counting

196   statistics but also errors on baseline subtraction and energy scaling) on parameters

197   derived from S. We applied the same algorithm to the new data reported here and to

198   the raw data reported in Dauphas et al. (2012).

199

200   **2.2. Computational methods**

201   Goethite (α-FeOOH) has an orthorhombic unit cell (a = 4.598 Å, b = 9.951 Å, c

202   = 3.018 Å, *Pbnm* space group, Yang et al. 2006), containing four formula units.

203   Calculations are done with the PWscf code (Giannozzi et al., 2009;

204   http://www.quantum-espresso.org) using the density functional theory (DFT) and the

205   generalized gradient approximation (GGA) to the exchange-correlation functional

206   with the PBE parameterization (Perdew et al. 1996). The ionic cores are described by

207   the ultrasoft pseudopotentials Fe.pbe-nd-rrkjus.UPF, O.pbe-rrkjus.UPF, H.pbe-

208   rrkjus.UPF, as in Blanchard et al. (2009, 2010, 2014). The wave-functions and the

209   charge density are expanded in plane-waves with 40 and 480 Ry cutoffs, respectively.

210   Increasing these energy cutoffs to 60 and 720 Ry does not modify significantly the

211   vibrational frequencies (< 1%). For the electronic integration, the Brillouin zone is

212   sampled according to the Monkhorst-Pack scheme (Monkhorst and Pack 1976), using

213   shifted $4 \times 2 \times 6$ *k*-point grids. Increasing the number of *k*-points does not modify the

214   structural and vibrational properties. Calculations are spin-polarized and set up to the

215   antiferromagnetic structure. The spins are oriented along the *c*-axis of goethite with

216   up and down spins in alternate chains of octahedra (Cornell and Schwertmann, 2003).

217   Magnetic moments are free to relax. Atomic positions are relaxed until the residual

218   forces on atoms are less than 10^{-4} Ry/a.u..

219   Additional calculations were performed using the GGA+U method since it is

220   known that the addition of a Hubbard U correction on the Fe atom improves the

221   description of the electronic and elastic properties of goethite by taking into account

222   the strong on-site Coulomb repulsion of Fe $3d$ electrons (*e.g.* Otte et al. 2009). The

223   value of the Hubbard U is determined using a linear response approach in an

224   internally consistent way following the procedure proposed by Cococcioni and de

225   Gironcoli (2005) and Kulik et al. (2006). Details about the practical procedure can be

226   found in Blanchard et al. (2008). The value of the Hubbard U is found equal to 3.34

227   eV, a value similar to the 3.30 eV found for hematite (Blanchard et al. 2008).

228   Following the method described in Blanchard et al. (2009), the β-factors were

229   calculated from the harmonic vibrational frequencies using

230
$$\beta(a,Y) = \left[\prod_{i=1}^{3N_{at}} \prod_{\{q\}} \frac{\nu_{q,i}^*}{\nu_{q,i}} \frac{e^{-h\nu_{q,i}^*/(2kT)}}{1-e^{-h\nu_{q,i}^*/(kT)}} \frac{1-e^{-h\nu_{q,i}/(kT)}}{e^{-h\nu_{q,i}/(2kT)}} \right]^{1/(N_qN)} \quad \text{(Eq. 6)}$$

231   where $\nu_{q,i}$ are the frequencies of the phonon with wavevector q and branch index i =

232   1,3N_{at}. N_{at} is the number of atoms in the unit cell, while $\nu_{q,i}$ and $\nu_{q,i}^*$ are the vibrational

233   frequencies in two isotopologues. N is the number of sites for the Y atom in the unit

234   cell, T is the temperature, h is the Planck constant and k is the Boltzmann constant.

235   Phonon frequencies were calculated within the harmonic approximation using the

236   linear response theory (Baroni et al. 2001, Floris et al. 2011) as implemented in the

237   PHonon code (Giannozzi et al., 2009; http://www.quantum-espresso.org). Phonon

238   frequencies were computed on shifted 2 × 2 × 2 q-point grids, for which the

239   convergence of the β-factors is achieved.

240   The β-factors calculated from the pDOS (Eq. 2) are identical to the β-factors

241   calculated directly from the harmonic vibrational frequencies (Eq. 6) providing that

242 the highest energy of the pDOS is smaller than $2\pi kT$. When it is not the case (*i.e.*

243 when OH stretching modes are considered in the pDOS) the formula derived from

244 perturbation theory (Eq. 1-4 in Polyakov et al. 2005) must be used instead.

245

246   **3. RESULTS**

247 **3.1. Reappraisal of NRIXS data**

248   The two motivations for implementing a non-constant baseline subtraction

249 procedure were that (1) replicate measurements of a given phase over several years

250 yielded force constant values that were not reproducible and (2) the signal at the low

251 and high energy ends of the spectrum often did not reach zero, so that the force

252 constant integral did not converge. In Fig. 1, we show force constant determinations

253 with or without baseline subtraction for goethite and jarosite. The values without

254 baseline subtraction were processed in the same manner as in Dauphas et al. (2012),

255 meaning that a constant background was subtracted, which is given by the average

256 counts measured in a 10 meV window at the low-energy end of the spectrum (*e.g.*,

257 from -130 to -120 meV). The values without baseline subtraction differ slightly from

258 those reported by Dauphas et al. (2012) and Hu et al. (2013) because we now only use

259 the phonon-creation side to calculate the force constant (the phonon-annihilation side

260 is calculated from the detailed balance and the temperature). The phonon annihilation

261 side is still measured to define the low-energy end of the baseline but this side of the

262 spectrum often suffers from low counting statistics, which is the reason why it is not

263 used to calculate the mean force constant. When no baseline is subtracted, the force

264 constant values show variations from one sample to another that far exceed individual

265 error bars (reduced $\chi^2 = 13.2$). When the data are corrected for the presence of a non-

266 constant baseline, the average force constant does not change but the sample-to-

267   sample scatter is very much reduced (reduced χ^2 = 3.1). The improvement in

268   reproducibility (Fig. 1) and better consistency with force constant estimates from

269   theory (see Sect. 3.2.1) justify our preference of the non-constant baseline data

270   reduction algorithm (Dauphas et al., 2014). Below, we discuss the results for each

271   phase individually.

272

273   *3.1.1. Goethite*

274   Including the measurements published by Dauphas et al. (2012), goethite was

275   analyzed by NRIXS three times. As explained in Dauphas et al. (2014) and the

276   method section, the main difference in the data reduction approach used here versus

277   that used by Dauphas et al. (2012) is the recognition that the non-zero signals at the

278   low- and high-energy ends of the spectrum are not from multiple phonons but rather

279   some non-constant baseline. Dauphas et al. (2012) used the counts at the low energy

280   end as baseline and interpreted the non-zero counts at the high-energy end to reflect

281   the presence of multiple phonons. Because the signal never reached zero for goethite,

282   a correction for missing multiple phonons was even applied, which exacerbated the

283   problem. The new approach removes a linear baseline interpolated between the low-

284   and high-energy ends of the spectrum using the SciPhon software (Dauphas et al.

285   2014). Various quantities calculated from *S(E)* and *g(E)* are compiled in Table 1. The

286   pDOS calculated for the three goethite samples are very reproducible and the average

287   pDOS is plotted in Fig. 2.

288   As shown in Table 1 and later in Table 5 for jarosite samples, B_2 (Eq. 4) is

289   almost the same for the phases investigated (~59,000), so the force constant is the

290   main controlling factor in iron isotopic fractionation even at low temperature and we

291   will focus on the values of the force constants in comparing the results obtained by

292   Dauphas et al. (2012) and Hu et al. (2013) with those presented here. The force

293   constant values obtained from g are identical to those obtained from S, so we will only

294   discuss the values obtained from S in the following.

295   For goethite, Dauphas et al. (2012) reported force constants of 307±9 N/m

296   from S and 314±10 N/m from S after refinement. Hu et al. (2013) obtained similar

297   values using the same data reduction approach. Significant signal remained at the

298   high-energy end and as a result the force constant integral did not plateau (Fig. 6 of

299   Dauphas et al., 2012), the new truncation-linear baseline subtraction protocol applied

300   to the same data (using SciPhon) leads to a significant reduction of the force constant,

301   *i.e.* 277±15 N/m. The larger error bar reflects the fact that additional sources of

302   uncertainties associated with baseline subtraction and energy scaling are propagated

303   in the calculation of the force constant (Hu et al. 2013, Dauphas et al. 2014). The two

304   new goethite measurements yield force constants of 264±13 N/m and 267±13 N/m,

305   averaging to 268±8 N/m for the three goethite measurements.

306

307   *3.1.2. Jarosite*

308   Including the measurements published by Dauphas et al (2012), hydronium

309   (H-) jarosite and potassium (K-) jarosite were analyzed twice each. Like for goethite,

310   various quantities calculated from S(E) and g(E), using the new data reduction

311   algorithm, are compiled in Table 2. The pDOS calculated for the two H-jarosite, and

312   two K-jarosite samples are very reproducible and the average pDOS are plotted in

313   Fig. 3.

314   The force constant for H-jarosite reported by Dauphas et al. (2012) was 302±9

315   N/m from S and 310±9 from S after refinement. Data reduction using SciPhon yields a

316   force constant for this sample of 273±15 N/m. A second measurement of this sample

317 during a different session gives 289±17 N/m. The average force constant for the two

318 H-jarosite measurements is 280±11 N/m.

319   The force constant of K-jarosite reported by Dauphas et al. (2012) was 262±6

320 N/m from S and 264±6 from S after refinement. The revised estimate using SciPhon

321 gives a force constant of 279±16 N/m. A second force constant measurement of this

322 sample during another session gives a force constant of 305±18 N/m. The average of

323 these two values is 290±12 N/m.

324   In the case of H-jarosite, for which significant signal remained at the high-

325 energy end and as a result the force constant integral did not converge (Fig. 6 of

326 Dauphas et al., 2012), the new data-reduction leads to a significant reduction of the

327 force constant. In the case of K-jarosite, the force constant integral plateaued and the

328 estimated force constant does not change significantly with the new data reduction

329 scheme used in SciPhon. Note that Dauphas et al. (2012) had no satisfactory

330 explanation as to why the force constant of H-jarosite was significantly higher than K-

331 jarosite, other than invoking the presence of high-energy modes arising from

332 hydrogen vibrations. The results presented here show that the force constants of H-

333 jarosite and K-jarosite are indistinguishable (280±11 N/m vs. 290±12 N/m).

334

335 **3.2. First-principles determination of isotopic fractionation properties**

336 *3.2.1. Iron β-factor of goethite*

337   In first-principles calculations, the goethite cell parameters were fixed to their

338 experimental values (Yang et al., 2006) and atomic positions were relaxed using

339 either GGA or GGA+U methods. GGA atomic positions are in excellent agreement

340 with the experimental values (Table 3). Only the x atomic coordinate of H atoms

341 shows a significant discrepancy revealing the difficulty of DFT to treat hydrogen

342 bonds as well as the difficulty to determine experimentally the H positions. The

343 GGA+U performs similarly as GGA for the description of interatomic distances

344 (Table 4). This is also true for the vibrational properties. We observe a good

345 correlation between experimental and theoretical frequencies for both GGA and

346 GGA+U methods (Fig. 4). As already highlighted in Blanchard et al. (2014), the

347 effect of the Hubbard U correction is mostly visible on the OH bending and stretching

348 modes. The OH bending frequencies increase while the OH stretching frequencies

349 decrease, consistently with lengthening of the O-H bond. The pDOS and in particular

350 the iron contribution is calculated using a $8 \times 4 \times 12$ q-points grid obtained through a

351 Fourier (trigonometric) interpolation of the force constants (see Méheut et al., 2007,

352 for details). We observe a general good agreement between the calculated and

353 measured iron pDOS (Fig. 2a). In detail, small differences can be noted between the

354 average measured pDOS and the calculated ones. These differences are of the same

355 order of magnitude as the differences between the pDOS computed with GGA and

356 GGA+U, and are distributed all along the energy range, which suggests that they are

357 not related to any specific vibrational modes. However, these small divergences lead

358 to a significant difference in the calculated iron force constants that are equal to 233

359 N/m and 247 N/m using GGA and GGA+U, respectively. The force constant is

360 calculated from the pDOS g by using equation (5). The integral in the second moment

361 of g explains why the OH vibration modes with their high energies contribute a little

362 to the iron force constant while the corresponding pDOS signal is almost negligible

363 (Fig. 2). The difference between the DFT (233 N/m for GGA, 247 N/m for GGA+U)

364 and NRIXS (268±8 N/m) force constants is already present before the OH vibration

365 modes. Calculations show that the pDOS should be exactly zero over a certain energy

366 range between the lattice modes and the OH bending modes (Fig. 2b), which is not

367   the case for the NRIXS measurements and contributes to the overestimation of the

368   iron force constant. This is likely due to the position of the baseline that should be

369   slightly higher. The variability of the calculated $^{57}Fe/^{54}Fe$ β-factor is shown in Fig. 5,

370   and the corresponding temperature dependences are reported in Tables 1 and 5. Its

371   variations follow variations in the iron force constant (Eq. 4). GGA and GGA+U

372   results differ by ~8 % and it is not possible from the analysis of the vibrational

373   properties to identify which computational method gives the best description of

374   goethite. This difference should thus give an idea of the uncertainty intrinsic of DFT.

375   These theoretical values are lower than the NRIXS-derived β-factor but higher than

376   the β-factor determined by Polyakov and Mineev (2000) from the Mössbauer

377   measurements done by de Grave and Vanderberghe (1986). Therefore with the new

378   NRIXS data reduction, the discrepancy between the various analytical approaches is

379   reduced but remains significant.

380   A general scaling factor reflecting the systematic underestimation of

381   vibrational frequencies by the GGA functional is sometimes applied (*e.g.* Schauble

382   2011) or a mineral-dependent scaling factor is taken, assuming an accurate

383   preliminary assignment of the vibrational modes (*e.g.* Blanchard et al. 2009). Here the

384   theoretical β-factors were obtained by fixing the cell parameters to the experimental

385   values and relaxing only the atomic positions. Following this procedure, we found

386   that the interatomic bond lengths and therefore the vibrational frequencies are

387   improved with respect to the fully optimized structure (*i.e.* relaxation of the cell

388   parameters and atomic positions). No further frequency correction is needed. The iron

389   β-factors of goethite calculated here are equal to 10.2 ‰ or 11.0 ‰ at 22°C, using

390   either GGA or GGA+U methods. These values compare well with 10.5 ‰, which is

391   the β-factor obtained from the fully relaxed structure and a frequency scale factor of

392 1.04 (quantified by taking the best linear-fit of the theoretical versus experimental

393 frequencies). The same approach was applied to hematite, by keeping fixed the cell

394 parameters of the rhombohedral primitive cell to the experimental values (a = 5.427

395 Å, α = 55.28°, $R\bar{3}c$ space group, Finger and Hazen, 1980). Unlike goethite, the

396 addition of the Hubbard U clearly improves the atomic positions, interatomic

397 distances and vibrational frequencies of hematite. Therefore, only GGA+U results are

398 retained and it is found that the new GGA+U iron β-factor is undistinguishable from

399 the β-factor previously published in Blanchard et al. (2009) where a frequency scale

400 factor of 1.083 was used. In a similar way, we checked for pyrite that the iron β-factor

401 obtained with the experimental cell parameters (Brostigen and Kjekshus, 1969), *i.e.*

402 13.1 ‰ at 22°C, is close, within the expected uncertainty, to the value calculated in

403 Blanchard et al. (2009), *i.e.* 13.6 ‰. However we would like to emphasize that fixing

404 the cell parameters to the experimental values do not dispense with checking that the

405 calculated frequencies are in good agreement with the measured values.

406

407 *3.2.2. Oxygen β-factor of goethite and hematite*

408 Beside iron β-factors, first-principles calculations provide the $^{18}O/^{16}O$ β-factor

409 of goethite as a function of temperature (Fig. 6 and Table 6). For goethite, GGA and

410 GGA+U results differ by ~4%. In the ideal goethite structure, half of the oxygen

411 atoms are hydroxylated and the others are not. Calculations show that these two

412 oxygen populations can be distinguished isotopically. At thermodynamic equilibrium,

413 heavier isotopes will concentrate preferentially in hydroxylated sites. The oxygen

414 isotope fractionation of goethite corresponds then to the average of all oxygen atoms

415 of the system. Similar calculations were also performed on hematite, using the same

416 model as that previously used by Blanchard et al. (2009). As explained in section

417 3.2.1, only GGA+U results are considered. With ~62 ‰ at 25 °C, the oxygen β-factor

418 of hematite is found to be very close to the one of goethite, but with a slightly more

419 linear temperature dependence (Fig. 6).

420

421 **4. DISCUSSION**

422 **4.1. Iron β-factor of goethite: intercomparison of the different methods**

423 In principle, DFT, NRIXS and Mössbauer spectroscopy should lead to

424 statistically undistinguishable iron β-factors. In the case of hematite, an excellent

425 agreement is found between DFT-derived $^{57}Fe/^{54}Fe$ β-factor (*i.e.* 10.9 ‰ at 22 °C,

426 Blanchard et al. 2009) and NRIXS-derived $^{57}Fe/^{54}Fe$ β-factor (*i.e.* 11.3 ± 0.4 ‰ at 22

427 °C, Dauphas et al. 2012). In the case of pyrite, the apparent discrepancy between DFT

428 and Mössbauer results that was reported in Blanchard et al. (2009) and in Polyakov

429 and Soultanov (2011), could be resolved by using a better constrained temperature

430 dependence of the Mössbauer spectra (Blanchard et al. 2012). The first NRIXS-based

431 estimation has recently confirmed our pyrite iron β-factor (Polyakov et al. 2013). In

432 light of these previous studies, it is essential to investigate the origin of the scattering

433 of the goethite iron β-factors obtained from the three analytical techniques.

434 The first obvious difference between goethite and hematite is the presence of

435 hydrogen atoms, and it is well known that the accurate description of hydrogen

436 bonding using DFT remains a concern. However, it is important to note that the

437 lengths of the Fe-O and Fe-OH bonds are well described (Table 4) and that all

438 vibrational frequencies below 700 cm^{-1} (*i.e.* excluding OH bending and stretching

439 modes) compare well with the experimental values (Fig. 4). These vibrational modes

440 are the main ones that contribute to the iron β-factor (Fig. 2c). The main difference

441 between GGA, GGA+U and NRIXS comes from the high-energy end of the lattice

442 modes (65 - 90 meV or 525 - 725 cm^{-1}) and the fact that the NRIXS pDOS does not

443 go down to zero between the lattice modes and OH bending modes (Fig. 2).

444   The nature and quality of the samples may also have an impact on iron isotope

445 composition. On one hand, a ^{57}Fe-rich sample with particle sizes of ~20 nm was

446 synthesized for the NRIXS measurements, and on the other hand, Mössbauer

447 spectroscopy was done on natural sample from the Harz mountains, well-crystallized

448 with particle size of ~1 μm (de Grave and Vandenberghe, 1986). Some kind of

449 internal disorder is however commonly observed in goethite, using *e.g.* differential

450 thermal analysis, infrared or magnetic measurements (Cornell and Schwertmann,

451 2003). This internal disorder may correspond to crystal defects and/or iron vacant

452 sites that are compensated for by extra, non-stoichiometric protons. All this amounts

453 to introducing distortions with respect to the ideal crystal structure. In "real" goethite

454 crystals, there will be a larger variation in the length of Fe-O bonds, which will lead to

455 a larger variation of the local iron *β*-factors (*i.e.* *β*-factors associated with each iron

456 atom). In a similar but simpler way, the ideal goethite structure displays already two

457 oxygen populations with specific isotopic signatures and the bulk oxygen *β*-factor

458 corresponds to the average of these two local *β*-factors (Fig. 6). The prediction of the

459 iron *β*-factor of a goethite crystal containing a certain amount of defects would

460 require the accurate characterization of the sample at the molecular scale, which is

461 beyond the scope of the present paper. It is noteworthy that the presence of defective

462 sites is not necessarily expressed in the overall isotopic composition because

463 compensation of local *β*-factors may occur. For instance, Blanchard et al. (2010)

464 investigated the isotopic properties of hematite with iron vacant sites compensated by

465 protons. The local iron *β*-factors display variations over a significant range (1.1 ‰ at

466 0 °C), but extreme values compensate each other, resulting for the model investigated,

467   in a negligible effect of these cationic vacancies on the iron isotope composition of

468   hematite. Similarly, we built a $2 \times 1 \times 2$ supercell of goethite containing one iron

469   vacancy compensated by three protons. The overall $^{57}Fe/^{54}Fe$ β-factor is almost

470   unchanged (11.99 ‰ instead of 11.94 ‰ at 0 °C using GGA), even if the local β-

471   factors display values ranging from 11.22 ‰ to 13.61 ‰ at 0 °C (the highest value,

472   *i.e.* 13.61 ‰, corresponds to an iron atom surrounded by two vacancies because of the

473   periodic repetition of the simulation cell).

474   Iron force constant and β-factor can also be affected by surface sites, the

475   contribution of which should depend on the size of the crystals. Unlike for defects in

476   bulk, the molecular relaxation in vicinity of the surfaces will more likely give rise to a

477   specific isotopic signature that will affect the overall isotopic composition. Beard et

478   al. (2010) and Frierdich et al. (2014) investigated the isotopic exchange between

479   aqueous Fe(II) and goethite, using two sizes of goethite. Their results demonstrate that

480   the equilibrium isotopic properties of nano-scale minerals may be distinct from

481   micron-scale or larger minerals. They found that iron surface sites are enriched in

482   heavy isotopes compared to bulk goethite. This fractionation is consistent with the

483   fact that the NRIXS-derived β-factor (for a nano-scale sample) is higher than the

484   Mössbauer-derived β-factor (for a micron-scale sample). However the difference

485   observed in β-factors (Fig. 5) is large compared to the difference in equilibrium

486   fractionation measured by Frierdich et al. (2014) for various particle sizes. Rustad and

487   Dixon (2009) examined iron isotope fractionation between hematite and aqueous iron,

488   and found almost no difference between bulk and surface β-factors. This conclusion

489   applies to the (012) hematite surface with molecularly and dissociatively adsorbed

490   water, using DFT calculations and the embedded cluster approach. Only few

491 experimental and theoretical data exist on the topic. More studies are needed with

492 other mineral surfaces and more structurally-complex surfaces.

493

494 **4.2. Isotopic fractionations between minerals (α-factors)**

495   The experimental iron isotope fractionation factors between goethite, hematite

496 and pyrite in condition of thermodynamic equilibrium can be determined by

497 combining the measurements from Skulan et al. (2002), Welch et al. (2003), Syverson

498 et al. (2013) and Frierdich et al. (2014) (Table 7). Keeping in mind that these mineral-

499 mineral isotopic fractionations do not represent direct measurements and involve

500 approximations like temperature extrapolations, we can compare them with the

501 equilibrium fractionation factors estimated from NRIXS, Mössbauer or DFT (Fig. 7).

502 The range of iron β-factors obtained for goethite (Fig. 5) leads to a significant spread

503 of iron α-factors for pyrite-goethite and hematite-goethite (Fig. 7). DFT α-factor is in

504 good agreement with the experimental pyrite-hematite value (0.62 ‰ compared to

505 $\Delta^{57}Fe = 0.44 \pm 1.0$ ‰ at 350 °C). For pyrite-goethite, DFT α-factors (GGA and

506 GGA+U) are within the error bar of the experimental data. For hematite-goethite,

507 DFT curves are 1-2 ‰ lower than the experimental points at 98 °C. The Mössbauer-

508 derived β-factor of goethite (Polyakov and Mineev 2000) seems to be in better

509 agreement with experimental points, while NRIXS data fall in the lowest part of the

510 range (*i.e.*, little iron isotopic fractionation between goethite and hematite). The same

511 conclusions could also be reached looking at the isotopic fractionation between

512 aqueous Fe(II) and goethite (Frierdich et al. 2014). However this would require to

513 combine the present mineral β-factors with a Fe(II)$_{aq}$ β-factor obtained from a

514 different technique (for instance, the DFT values from Rustad et al., 2010, currently

515 considered as the most reliable, and based on an aperiodic model, B3LYP exchange-

516   correlation functional and localized basis sets). This practice should be considered

517   with caution and the combination of β-factors determined by a single methodology is

518   always preferable.

519   It often happens that the iron β-factors derived from Mössbauer are slightly different

520   and lower than the ones derived from NRIXS, but usually when the α-factors are

521   determined the agreement between these two methods and with the experimental data

522   is satisfactory. This is shown, for instance, for the isotopic fractionation between

523   molten silicate, FeS and metal (Dauphas et al., 2014).

524   For the oxygen isotopes, DFT results (GGA and GGA+U) indicate a small

525   equilibrium fractionation between hematite and goethite (between -3.1 and +0.8 ‰

526   over the whole temperature range, Fig. 8). These theoretical estimations are consistent

527   with the study of Yapp (1990), which suggests, from synthesis experiments conducted

528   in the temperature range 25-120 °C, that goethite and hematite are isotopically

529   indistinguishable at equilibrium. Several experimental studies also investigated

530   oxygen isotope fractionation in hematite-water and goethite-water systems (*e.g.* Bao

531   and Koch, 1999; Yapp, 2007). The hematite-goethite fractionation curve that can be

532   derived from Bao and Koch (1999) shows a similar temperature-dependence as our

533   GGA results but is slightly more positive (Fig. 8). In this study, experiments of

534   goethite synthesis were performed at a pH higher than 14. However Yapp's results

535   (2007) suggest that, in addition to temperature, pH can affect the measured oxygen

536   isotope fractionation between goethite and water. He found for goethite synthesized at

537   low pH (~1 to 2) a curve that differs significantly from the ones obtained at high pH

538   (>14). Using this low-pH curve for goethite-water from Yapp (2007) and the

539   hematite-water oxygen fractionation from Bao and Koch (1999), the hematite-goethite

540   fractionation curve falls in the range predicted by DFT methods but with an stronger

541　temperature-dependence (Fig. 8). According to Yapp (2007), data measured for

542　goethite crystallized at low pH may approach isotopic equilibrium values. These data

543　are therefore the ones that must be compared preferentially with the DFT results. In

544　conclusion, theoretical estimations for oxygen isotopes are consistent with

545　experimental measurements, even if the exact temperature-dependence remains

546　uncertain.

547　Our data display a significant discrepancy with the results of the semi-empirical

548　approach of Zheng (1991, 1998), *i.e.* the modified increment method where the

549　equilibrium oxygen isotope fractionation factors of oxides are assessed with respect to

550　a reference mineral (quartz) by considering the bond-type in the crystal structure (*e.g.*,

551　bond strength, effect of mass on isotopic substitution). Blanchard et al. (2010) already

552　reported a discrepancy for the oxygen isotope fractionation between hematite and

553　corundum, suggesting that the modified increment method cannot be used to reliably

554　predict isotopic fractionation factors.

555

565

REFERENCES

565

566 Bao H. and Koch P.L. (1999) Oxygen isotope fractionation in ferric oxide-water

567   systems: Low temperature synthesis. *Geochim. Cosmochim. Acta* **63**, 599-613.

568 Baroni S., de Gironcoli S., Dal Corso A. and Giannozzi P. (2001) Phonons and related

569   crystal properties from density-functional perturbation theory. *Rev. Mod. Phys.*

570   **73**, 515-561.

571 Beard B. L., Handler R. M., Scherer M. M., Wu L., Czaja A. D., Heimann A. and

572   Johnson C. M. (2010) Iron isotope fractionation between aqueous ferrous iron

573   and goethite. *Earth Planet. Sci. Lett*. **295**, 241-250.

574 Blanchard M., Lazzeri M., Mauri F. and Balan E. (2008) First-principles calculation

575   of the infrared spectrum of hematite. *Am. Mineral*. **93**, 1019-1027.

576 Blanchard M., Poitrasson F., Méheut M., Lazzeri M., Mauri F. and Balan E. (2009)

577   Iron isotope fractionation between pyrite (FeS_2), hematite (Fe_2O_3) and siderite

578   ($FeCO_3$): a first-principles density-functional theory study. *Geochim. Cosmochim.*

579   *Acta* **73**, 6565–6578.

580 Blanchard M., Morin G., Lazzeri M. and Balan E. (2010) First-principles study of the

581   structural and isotopic properties of Al- and OH-bearing hematite. *Geochim.*

582   *Cosmochim. Acta* **74**, 3948-3962.

583 Blanchard M., Poitrasson F., Méheut M., Lazzeri M., Mauri F. and Balan E. (2012)

584   Comment on "New data on equilibrium iron isotope fractionation among sulfides:

585   Constraints on mechanisms of sulfide formation in hydrothermal and igneous

586   systems" by V.B. Polyakov and D.M. Soultanov. *Geochim. Cosmochim. Acta*, **87**,

587   356-359.

588 Blanchard M., Balan E., Giura P., Béneut K., Yi H., Morin G., Pinilla C., Lazzeri M.

589   and Floris A. (2014) Infrared spectroscopic properties of goethite: anharmonic

590   broadening, long-range electrostatic effects and Al substitution. *Phys. Chem.*

591   *Minerals*, **41**, 289-302.

592   Brostigen G. and Kjekshus A. (1969) Redetermined crystal structure of FeS_2 (pyrite).

593   *Acta Chem. Scand.*, **23**, 2186–2188.

594   Cambier P. (1986) Infrared study of goethites of varying crystallinity and particle

595   size: I. Interpretation of OH and lattice frequencies. *Clay Minerals* **21**, 191-200.

596   Cococcioni M. and de Gironcoli S. (2005) Linear response approach to the calculation

597   of the effective interaction parameters in the LDA+U method. *Phys. Rev. B* **71**,

598   035105.

599   Cornell R. M. and Schwertmann U. (2003) The iron oxides: structure, properties,

600   reactions, occurrences and uses. 2nd ed., Wiley-VCH, pp. 664

601   Dauphas N., Roskosz M., Alp E. E., Golden D. C., Sio C. K., Tissot F. L. H., Hu M.

602   Y., Zhao J., Gao L. and Morris R. V. (2012) A *general moment* NRIXS approach

603   to the determination of equilibrium Fe isotopic fractionation factors: Application

604   to goethite and jarosite. *Geochim. Cosmochim. Acta* **94**, 254-275

605   Dauphas N., Roskosz M., Alp E. E., Neuville D., Hu M., Sio C. K., Tissot F. L. H.,

606   Zhao J., Tissandier L., Medard E. and Cordier C. (2014) Magma redox and

607   structural controls on iron isotope variations in Earth's mantle and crust. *Earth*

608   *Planet. Sci. Lett.*, **398**, 127-140

609   de Faria D. L. A. and Lopes F. N. (2007) Heated goethite and natural hematite: Can

610   Raman spectroscopy be used to differentiate them? *Vibrational spectroscopy* **45,**

611   117-121.

612   de Grave E. and Vandenberghe R. E. (1986) [57]Fe Mössbauer effect study of well-

613   crystalized goethite (α-FeOOH). *Hyperfine Interactions* **28**, 643-646.

614   Eiler J. M., Bergquist B., Bourg I., Cartigny P., Farquhar J., Gagnon A., Guo W.,

615   Halevy I., Hofmann A., Larson T. E., Levin N., Schauble E. A. and Stolper D.

616   (2014) Frontiers of stable isotope geoscience. *Chem. Geol.* **373**, 119-143.

617   Finger L. W. and Hazen R. M. (1980) Crystal structure and isothermal compression of

618   Fe_2O_3, Cr_2O_3, and V_2O_3 to 50 kbars. *J. Appl. Phys.* **51**, 5362–5367.

619   Floris A., de Gironcoli S., Gross E. K. U. and Cococcioni M. (2011) Vibrational

620   properties of MnO and NiO from DFT+U-based Density Functional Perturbation

621   Theory, *Phys. Rev. B* **84**, 161102(R).

622   Frierdich A. J., Beard B. L., Reddy T. R., Scherer M. M. and Johnson C. M. (2014)

623   Iron isotope fractionation between aqueous Fe(II) and goethite revisited: New

624   insights based on a multi-direction approach to equilibrium and isotopic exchange

625   rate modification. *Geochim. Cosmochim. Acta.* **139,** 383-398.

626   Giannozzi P., Baroni S., Bonini N., Calandra M., Car R., Cavazzoni C., Ceresoli D.,

627   Chiarotti G. L., Cococcioni M., Dabo I., Dal Corso A., de Gironcoli S., Fabris S.,

628   Fratesi G., Gebauer R., Gerstmann U., Gougoussis C., Kokalj A., Lazzeri M.,

629   Martin-Samos L., Marzari N., Mauri F., Mazzarello R., Paolini S., Pasquarello

630   A., Paulatto L., Sbraccia C., Scandolo S., Sclauzero G., Seitsonen A. P.,

631   Smogunov A., Umari P. and Wentzcovitch R. M. (2009) Quantum ESPRESSO: a

632   modular and open-source software project for quantum simulations of materials.

633   *J. Phys.: Conden.s Matter* **21**, 395502.

634   Golden D. C., Ming D. W., Morris R. V. and Graff T. G. (2008) Hydrothermal

635   synthesis of hematite spherules and jarosite: Implications for diagenesis and

636   hematite spherule formation in sulfate outcrops at Meridiani Planum, Mars. *Am.*

637   *Mineral.* **93**, 1201–1214.

638   Hu M., Sturhahn Y. W., Toellner T. S., Mannheim P. D., Brown D. E., Zhao J. and

639   Alp E. E. (2003) Measuring velocity of sound with nuclear resonant inelastic x-

ray scattering, *Phys. Rev. B* **67**, 094304.

Hu M. Y., Toellner T. S., Dauphas N., Alp E. E. and Zhao J. (2013) Moments in nuclear resonant inelastic x-ray scattering and their applications. *Phys. Rev. B* **87**, 064301

Johnson C. M., Beard B. L. and Albarède F. (2004) Geochemistry of non-traditional isotopes. *Rev. Mineral. Geochem.*, vol. **55**. Mineralogical Society of America, Geochemical Society. 454 p.

Johnson D. W. and Spence J. C. H. (1974) Determination of the single-scattering probability distribution from plural-scattering data. *J. Phys. D: Applied Physics* **7**, 771-780.

Kohn V. G. and Chumakov A. I. (2000) DOS: Evaluation of phonon density of states from nuclear resonant inelastic absorption. *Hyperfine Interactions* **125**, 205-221.

Kulik H. J., Cococcioni M., Scherlis D. A. and Marzari N. (2006) Density functional theory in transition-metal chemistry: a self-consistent Hubbard U approach. *Phys. Rev. Lett.* **97** ,103001.

Méheut M., Lazzeri M., Balan E. and Mauri F. (2007) Equilibrium isotopic fractionation in the kaolinite, quartz, water system: Prediction from first-principles density-functional theory. *Geochim. Cosmochim. Acta* **71**, 3170-3181.

Monkhorst H. J. and Pack J. D. (1976) Special points for Brillouin-zone integrations. *Phys. Rev. B* **13**, 5188-5192.

Otte K., Pentcheva R., Schmahl W. W. and Rustad J. R. (2009) Pressure-induced structural and electronic transitions in FeOOH from first- principles. *Phys. Rev. B* **80**, 205116.

Perdew J. P., Burke K. and Ernzerhof M. (1996) Generalized gradient approximation made simple. *Phys. Rev. Lett.* **77**, 3865–3868.

665   Polyakov V. B. and Mineev S. D. (2000) The use of Mössbauer spectroscopy in stable

666   isotope geochemistry. *Geochim. Cosmochim. Acta* **64**, 849-865.

667   Polyakov V. B., Mineev S. D., Clayton R. N., Hu G. and Mineev K. S. (2005)

668   Determination of tin equilibrium isotope fractionation factors from synchroton

669   radiation experiments. *Geochim. Cosmochim. Acta* **69**, 5531-5536.

670   Polyakov V. B., Clayton R. N., Horita J. and Mineev S. D. (2007) Equilibrium iron

671   isotope fractionation factors of minerals: Reevaluation from the data of nuclear

672   inelastic resonant X-ray scattering and Mössbauer spectroscopy. *Geochim.*

673   *Cosmochim. Acta* **71**, 3833-3846.

674   Polyakov V. B. and Soultanov D. M. (2011) New data on equilibrium iron isotope

675   fractionation among sulfides: Constraints on mechanisms of sulfide formation in

676   hydrothermal and igneous systems. *Geochim. Cosmochim. Acta* **75**, 1957-1974.

677   Polyakov V. B., Osadchii E. G., Chareev D. A., Chumakov A. I. and Sergeev I. A.

678   (2013) Fe β-factors for sulfides from NRIXS synchrotron experiments. *Mineral.*

679   *Mag.*, **77**, 1985.

680   Rustad J.R. and Dixon D.A. (2009) Prediction of iron-isotope fractionation between

681   hematite (α-Fe_2O_3) and ferric and ferrous iron in aqueous solution from Density

682   Functional Theory. *J. Phys. Chem. A*, **113**, 12249-12255.

683   Rustad J.R., Casey W.H., Yin Q-Z., Bylaska E.J., Felmy A.R., Bogatko S.A., Jackson

684   V.E. and Dixon D.A. (2010) Isotopic fractionation of Mg^{2+}(aq), Ca^{2+}(aq), and

685   Fe^{2+}(aq) with carbonate minerals. *Geochim. Cosmochim. Acta* **74**, 6301-6323.

686   Schauble E. A. (2011) First-principles estimates of equilibrium magnesium isotope

687   fractionation in silicate, oxide, carbonate and hexaaquamagnesium(2+) crystals.

688   *Geochim. Cosmochim. Acta* **75**, 844-869.

689   Seto M., Yoda Y., Kikuta S., Zhang X. W. and Ando M. (1995) Observation of

690   nuclear resonant scattering accompanied by phonon excitation using synchrotron

691   radiation. *Phys. Rev. Lett*. **74**, 3828-3831.

692   Skulan J. L., Beard B. L. and Johnson C. M. (2002) Kinetic and equilibrium Fe

693   isotope fractionation between aqueous Fe(III) and hematite. *Geochim.*

694   *Cosmochim. Acta* **66**, 2995–3015.

695   Sturhahn W., Toellner T. S., Alp E. E., Zhang X., Ando M., Yoda Y., Kikuta S., Seto

696   M., Kimball C. W. and Dabrowski B. (1995) Phonon density of states measured

697   by inelastic nuclear resonant scattering. *Phys. Rev. Lett*. **74**, 3832-3835.

698   Sturhahn W. (2000) CONUSS and PHOENIX: Evaluation of nuclear resonant

699   scattering data. *Hyperfine Interactions* **125**, 149-172.

700   Sturhahn W. and Jackson J. M. (2007) Geophysical applications of nuclear resonant

701   scattering, in Ohtani, E., ed., *Advances in High-Pressure Mineralogy: GSA*

702   *Special Paper* **421**, 157-174.

703   Syverson D. D., Borrock D. M. and Seyfried Jr. W. E. (2013) Experimental

704   determination of equilibrium Fe isotopic fractionation between pyrite and

705   dissolved Fe under hydrothermal conditions. *Geochim. Cosmochim. Acta* **122**,

706   170-183.

707   Valley J. W. and Cole D. R. (2001) Stable isotope geochemistry. *Rev. Mineral.*

708   *Geochem.*, vol. **43**. Mineralogical Society of America, Geochemical Society. 662

709   p.

710   Welch S. A., Beard B. L., Johnson C. M. and Braterman P. S. (2003) Kinetic and

711   equilibrium Fe isotope fractionation between aqueous Fe(II) and Fe(III).

712   *Geochim. Cosmochim. Acta* **67**, 4231–4250.

713   Yang H., Lu R., Downs R. T., Costin G. (2006) Goethite, α-FeO(OH), from single-

714   crystal data. *Acta Crystallographica* **E62**, i250-i252.

715   Yapp C. J. (1990) Oxygen isotopes in iron (III) oxides, 1. Mineral-water fractionation

716   factors. *Chem. Geol.* **85**, 329-335.

717   Yapp C. J. (2007) Oxygen isotopes in synthetic goethite and a model for the apparent

718   pH dependence of goethite-water $^{18}O/^{16}O$ fractionation. *Geochim. Cosmochim.*

719   *Acta* **71**, 1115-1129.

720   Zheng Y. F. (1991) Calculation of oxygen isotope fractionation in metal oxides.

721   *Geochim. Cosmochim. Acta* **55**, 2299-2307.

722   Zheng Y. F. (1998) Oxygen isotope fractionation between hydroxide minerals and

723   water. *Phys. Chem. Minerals* **25**, 213-221.

724

725 **TABLES**

726 **Table 1**. Goethite properties derived from NRIXS, based on the scattering spectrum, $S(E)$, or the projected partial phonon density of states, $g(E)$.

	Goethite 1			Goethite 2			Goethite 3			Mean for Goethite		
Parameters from S												
Temperature from detailed balance (K)	287			302			296			*295*		
Lamb-Mössbauer factor from S	0.7741	±	0.0026	0.7548	±	0.0020	0.7604	±	0.0020	*0.7614*	±	*0.0012*
Mean square displacement $<z^2>$ from S (Å^2)	0.00481	±	0.00006	0.00528	±	0.00005	0.00514	±	0.00004	*0.00511*	±	*0.00003*
Internal energy/atom from S (meV)	29.00	±	0.73	29.17	±	0.67	28.95	±	0.67	*29.04*	±	*0.40*
Kinetic energy/atom from S (meV)	14.50	±	0.37	14.58	±	0.34	14.48	±	0.34	*14.52*	±	*0.20*
Force constant from S (N/m)	277	±	15	264	±	13	267	±	13	*268*	±	*8*
(without truncation/baseline subtraction)	(319	±	17)	(250	±	16)	(260	±	14)			
$^{56}Fe/^{54}Fe$ β coefficients from S												
$1000 \ln \beta = A_1/T^2 + A_2/T^4 + A_3/T^6$ (T in K)												
A_1	7.898E+05	±	4.384E+04	7.537E+05	±	3.755E+04	7.605E+05	±	3.724E+04	*7.659E+05*	±	*2.264E+04*
A_2	-5.074E+09	±	6.634E+08	-5.382E+09	±	7.678E+08	-5.474E+09	±	6.729E+08	*-5.301E+09*	±	*4.024E+08*
A_3	7.516E+13	±	1.866E+13	1.154E+14	±	3.225E+13	1.111E+14	±	2.430E+13	*9.318E+13*	±	*1.345E+13*
$1000 \ln \beta = B_1<F>/T^2 - B_2<F>^2/T^4$ (T in K)												
B_1	2853			2853			2853			*2853*		
B_2	55630			59269			60154			*58351*		
Parameters from g												
Lamb-Mössbauer factor from g	0.7740			0.7546			0.7602			*0.7629*		
Mean square displacement $<z^2>$ from g (Å^2)	0.00481			0.00528			0.00515			*0.00508*		
$d<z^2>/dT$ (Å^2/K)	1.45E-05			1.60E-05			1.56E-05			*1.54E-05*		
Critical temperature (K)	1295			1170			1203			*1222*		
Resilience (N/m)	95			86			88			*90*		
Internal energy/atom from g (meV)	29.76			29.92			29.70			*29.80*		
Kinetic energy/atom from g (meV)	14.88			14.96			14.85			*14.90*		
Vibrational entropy (kb/atom)	1.00			1.05			1.03			*1.03*		
Helmholtz free energy (meV)	3.89			2.60			2.86			*3.12*		
Vibrational specific heat (kb/atom)	0.87			0.89			0.88			*0.88*		
Lamb-Mössbauer factor at T=0	0.92			0.92			0.92			*0.92*		
Kinetic energy/atom at T=0 (meV)	7.91			7.68			7.69			*7.76*		
Force constant from g (N/m)	276			262			266			*268*		

$^{56}Fe/^{54}Fe$ β coefficients from g

$1000 \ln \beta = A_1/T^2 + A_2/T^4 + A_3/T^6$ (T in K)

A_1	7.884E+05	7.490E+05	7.580E+05	*7.652E+05*
A_2	-5.060E+09	-5.333E+09	-5.442E+09	*-5.278E+09*
A_3	7.814E+13	1.158E+14	1.128E+14	*1.023E+14*
Velocities from g				
Input density (g/cc)	4.27	4.27	4.27	*4.27*
Input bulk modulus (GPa)	108.5	108.5	108.5	*108.5*
Debye velocity (m/s)	3934 ± 43	3808 ± 39	3899 ± 46	*3874 ± 25*
p-wave velocity (m/s)	6480 ± 29	6395 ± 26	6456 ± 31	*6439 ± 17*
s-wave velocity (m/s)	3526 ± 41	3409 ± 37	3493 ± 44	*3470 ± 23*
Poisson ratio	0.290	0.302	0.293	*0.295*

727

728

729

730

731

732

733

734

735

736

737 **Table 2**. Hydronium-jarosite and potassium-jarosite properties derived from NRIXS, based on the scattering spectrum, S(E), or the projected

738 partial phonon density of states, g(E).

	H-Jarosite 1			H-Jarosite 2			Mean for H-Jarosite			K-Jarosite 1			K-Jarosite 2			Mean for K-Jarosite		
Parameters from S																		
Temperature from detailed balance (K)	300			297			**298**			302			304			**303**		
Lamb-Mössbauer factor from S	0.6576	±	0.0023	0.6415	±	0.0022	**0.6492**	±	**0.0016**	0.6920	±	0.0016	0.6724	±	0.0018	**0.6832**	±	**0.0012**
Mean square displacement $\langle z^2 \rangle$ from S (Å^2)	0.00787	±	0.00006	0.00833	±	0.00006	**0.00810**	±	**0.00004**	0.00691	±	0.00004	0.00745	±	0.00005	**0.00715**	±	**0.00003**
Internal energy/atom from S (meV)	29.58	±	0.74	29.59	±	0.74	**29.59**	±	**0.52**	29.70	±	0.73	29.92	±	0.73	**29.81**	±	**0.52**
Kinetic energy/atom from S (meV)	14.79	±	0.37	14.80	±	0.37	**14.79**	±	**0.26**	14.85	±	0.37	14.96	±	0.37	**14.90**	±	**0.26**
Force constant from S (N/m) (without truncation/baseline subtraction)	273	±	15	289	±	17	**280**	±	**11**	279	±	16	305	±	18	**290**	±	**12**
	(316	±	17)	(241	±	20)				(281	±	13)	(294	±	17)			
$^{56}\text{Fe}/^{54}\text{Fe}$ β coefficients from S																		
$1000 \ln \beta = A_1/T^2 + A_2/T^4 + A_3/T^6$ (T in K)																		
A_1	7.778E+05	±	4.156E+04	8.254E+05	±	4.881E+04	**7.979E+05**	±	**3.164E+04**	7.951E+05	±	4.551E+04	8.705E+05	±	5.071E+04	**8.287E+05**	±	**3.387E+04**
A_2	-4.864E+09	±	5.725E+08	-7.939E+09	±	1.150E+09	**-5.475E+09**	±	**5.126E+08**	-5.208E+09	±	9.136E+08	-8.989E+09	±	1.444E+09	**-6.289E+09**	±	**7.720E+08**
A_3	6.032E+	±	1.438E+	2.269E+	±	5.105E+	**7.257E+**	±	**1.384E+**	8.178E+	±	3.445E+	2.941E+	±	7.686E+	**1.173E+**	±	**3.143E+**

	13	13	14	13	**13**	**13**	13	13	14	13	**14**	**13**
$1000 \ln \beta = B_1\langle F\rangle/T^2 - B_2\langle F\rangle^2/T^4$ (T in K)												
B_1	2853		2853		**2853**		2853		2853		**2853**	
B_2	56692		65584		**61138**		55698		62457		**59078**	
Parameters from g												
Lamb-Mössbauer factor from g	0.6569		0.6404		**0.6487**		0.6914		0.6716		**0.6815**	
Mean square displacement $\langle z^2\rangle$ from g (Å^2)	0.00789		0.00836		**0.00812**		0.00692		0.00747		**0.00720**	
$d\langle z^2\rangle/dT$ (Å^2/K)	2.47E-05		2.63E-05		**2.55E-05**		2.15E-05		2.33E-05		**2.24E-05**	
Critical temperature (K)	760		714		**737**		873		805		**839**	
Resilience (N/m)	56		53		**54**		64		59		**62**	
Internal energy/atom from g (meV)	30.24		30.25		**30.24**		30.39		30.61		**30.50**	
Kinetic energy/atom from g (meV)	15.12		15.12		**15.12**		15.20		15.30		**15.25**	
Vibrational entropy (kb/atom)	1.12		1.13		**1.13**		1.09		1.10		**1.10**	
Helmholtz free energy (meV)	1.17		0.90		**1.03**		2.08		2.05		**2.06**	
Vibrational specific heat (kb/atom)	0.89		0.89		**0.89**		0.89		0.89		**0.89**	
Lamb-Mössbauer factor at T=0	0.91		0.90		**0.91**		0.91		0.91		**0.91**	
Kinetic energy/atom at T=0 (meV)	7.69		7.67		**7.68**		7.84		7.93		**7.88**	
Force constant from g (N/m)	271		288		**279**		276		303		**290**	

^{56}Fe/^{54}Fe β

coefficients from g

$1000 \ln \beta = A_1/T^2 + A_2/T^4 + A_3/T^6$ (T in K)

A_1	7.721E+05	8.208E+05	**7.964E+05**	7.882E+05	8.642E+05	**8.262E+05**
A_2	-4.840E+09	-7.911E+09	**-6.375E+09**	-5.151E+09	-8.936E+09	**-7.043E+09**
A_3	6.296E+13	2.306E+14	**1.468E+14**	8.212E+13	2.962E+14	**1.891E+14**
Velocities from g						
Input density (g/cc)	3	3	**3**	3.25	3.25	**3.25**
Input bulk modulus (GPa)	56	56	**56**	56	56	**56**
Debye velocity (m/s)	3364 ± 134	3173 ± 40	**3189 ± 39**	3566 ± 104	3275 ± 50	**3330 ± 45**
p-wave velocity (m/s)	5549 ± 91	5422 ± 26	**5432 ± 25**	5567 ± 74	5360 ± 34	**5397 ± 31**
s-wave velocity (m/s)	3015 ± 128	2837 ± 38	**2852 ± 37**	3212 ± 99	2937 ± 48	**2989 ± 43**
Poisson ratio	0.291	0.312	**0.301**	0.250	0.285	**0.268**

739

Table 3. Theoretical and experimental atomic coordinates [±(x,y,3/4),

±(1/2+x,1/2+y,1/4)] of goethite. Values in brackets give the differences with respect

to the experimental values.

	xFe	yFe	xH	yH	xO	yO	xOh	yOh
GGA	0.0503	0.8523	0.4041	0.0855	0.6978	0.2001	0.1989	0.0528
	(0.001)	(-0.001)	(0.026)	(0.004)	(-0.008)	(0.001)	(0.000)	(0.000)
GGA+U	0.0603	0.8559	0.4011	0.0940	0.6798	0.1946	0.1959	0.0570
	(0.011)	(0.002)	(0.023)	(0.012)	(-0.026)	(-0.005)	(-0.003)	(0.004)
Exp.*	0.0489	0.8537	0.3781	0.0817	0.7057	0.1991	0.1987	0.0530

*Yang et al. (2006)

Table 4. Theoretical and experimental interatomic distances (Å). Values in brackets

give the differences with respect to the experimental values.

	Fe-O	Fe-Oh	O-H
GGA	1.8963 (-0.037)	2.1091 (0.010)	0.9975 (0.125)
	1.9725 (0.017)	2.1167 (0.011)	
GGA+U	1.9484 (0.015)	2.0958 (-0.004)	1.0130 (0.140)
	1.9889 (0.033)	2.1018 (-0.004)	
Exp.*	1.9332	2.0994	0.8729
	1.9560	2.1059	

*Yang et al. (2006)

Table 5. Fits of the calculated $10^3 \ln \beta$ based on the function $ax + bx^2 + cx^3$, with $x =$

$10^6/T^2$ (T on K) for $^{57}Fe/^{54}Fe$ isotope fractionation in goethite.

	a	b	c
GGA	9.384×10^{-1}	-4.7789×10^{-3}	4.9888×10^{-5}
GGA+U	10.248×10^{-1}	-5.8539×10^{-3}	6.8122×10^{-5}

756 **Table 6**. Fits of the calculated $10^3 \ln \beta$ based on the function $ax + bx^2 + cx^3$, with $x =$

757 $10^6/T^2$ (T on K) for $^{18}O/^{16}O$ isotope fractionation in goethite and hematite.

		a	b	c
Goethite O total	GGA	6.9558	-1.9730×10^{-1}	5.7833×10^{-3}
Goethite O total	GGA+U	7.1664	-1.8753×10^{-1}	5.2786×10^{-3}
Goethite O	GGA	5.2325	-4.2571×10^{-2}	4.3992×10^{-4}
Goethite O	GGA+U	5.5402	-4.9704×10^{-2}	5.8375×10^{-4}
Goethite Oh	GGA	8.6748	-3.5227×10^{-1}	1.1134×10^{-2}
Goethite Oh	GGA+U	8.7932	-3.2570×10^{-1}	9.9755×10^{-3}
Hematite O	GGA+U	6.0030	-5.1020×10^{-2}	5.1786×10^{-4}

758

759

760 **Table 7**. Mineral-mineral iron isotope fractionations determined from experimental

761 measurements. The extrapolation to higher temperature is made assuming a linear

762 dependence as a function of $10^6/T^2$ and a fractionation equal to zero at infinite

763 temperature. $\Delta^{56}Fe$ shown here are subsequently converted in $\Delta^{57}Fe$ for comparison in

764 Fig. 6.

Pyrite-Fe(II)$_{aq}$ Syverson et al. (2013)	**Fe(II)$_{aq}$-Goethite** Frierdich et al. (2014)		**Pyrite-Goethite**
0.99 ± 0.3 ‰ at 350 °C	-0.23 ± 0.1 ‰ -0.27 ± 0.1 ‰* extrapol. to 350 °C		0.76 ± 0.3 ‰ 0.72 ± 0.3 ‰ at 350 °C
Hematite-Fe(III)$_{aq}$ Skulan et al. (2002)	**Fe(III)$_{aq}$-Fe(II)$_{aq}$** Welch et al. (2003)	**Fe(II)$_{aq}$-Goethite** Frierdich et al. (2014)	**Hematite-Goethite**
0.1 ± 0.2 ‰ at 98 °C	1.87 ± 0.2 ‰ extrapol. to 98 °C	-0.66 ± 0.1 ‰ -0.77 ± 0.1 ‰* extrapol. to 98 °C	1.31 ± 0.3 ‰ 1.2 ± 0.3 ‰ at 98 °C
Pyrite-Fe(II)$_{aq}$ Syverson et al. (2013)	**Fe(II)$_{aq}$-Fe(III)$_{aq}$** Welch et al. (2003)	**Fe(III)$_{aq}$-Hematite** Skulan et al. (2002)	**Pyrite-Hematite**
0.99 ± 0.3 ‰ at 350 °C	-0.66 ± 0.2 ‰ extrapol. to 350 °C	-0.04 ± 0.2 ‰ extrapol. to 350 °C	0.29 ± 0.4 ‰ at 350 °C

765 * smaller particles

766

Figure Captions

767

768　**Figure 1.** Comparison between iron mean force constant determinations by NRIXS

769　with or without baseline subtraction. The baseline is a linear interpolation between

770　signal measured at the low- and high-energy ends of the NRIXS spectrum, where no

771　phonon contributions are expected. Baseline subtraction yields force constant values

772　that display better long-term reproducibility compared to no baseline subtraction (the

773　different replicates were measured at during several beamline sessions spanning three

774　years).

775

776　**Figure 2.** (a) Average measured (NRIXS) and calculated (GGA, GGA+U) phonon

777　density of states (pDOS) of iron atoms in goethite. (b) The iron pDOS and total pDOS

778　calculated with GGA are plotted along with the calculated (circles) and experimental

779　(triangles) infrared and Raman frequencies (Cambier, 1986; de Faria and Lopes,

780　2007). This highlights the energy gap existing between lattice modes and OH bending

781　modes. (c, d) The force constant is calculated from the pDOS by using the formula

782　$\langle F \rangle = \dfrac{M}{\hbar^2} \int_0^\lambda g(E) E^2 dE$, with the upper limit $\lambda = \infty$ (Eq. 5). The term $g(E)E^2$ is

783　plotted in (c), while the force constant integral for different values of the integration

784　upper-limit is plotted in (d).

785

786　**Figure 3.** Average phonon density of states of iron atoms in hydronium-jarosite and

787　potassium-jarosite measured using NRIXS.

788

789　**Figure 4.** Calculated (GGA and GGA+U) versus experimental infrared and Raman

790　frequencies of goethite (Cambier, 1986; de Faria and Lopes, 2007).

791

792 **Figure 5.** Temperature dependence of the iron β-factor of goethite.

793

794 **Figure 6.** Temperature dependence of the oxygen β-factor of goethite and hematite.

795

796 **Figure 7.** Temperature dependence of the iron α-factor between pyrite and goethite,

797 and between hematite and goethite. The experimental points have not been measured

798 directly and are estimated instead from several experiments, which are compiled in

799 Table 7 (Skulan et al., 2002; Welch et al., 2003; Syverson et al., 2013; Frierdich et al.,

800 2014). For Mössbauer, pyrite, hematite and goethite data are taken from Blanchard et

801 al. (2012), Polyakov et al. (2007) and Polyakov and Mineev (2000), respectively. For

802 GGA and GGA+U, pyrite and hematite data are from Blanchard et al. (2009) while

803 goethite data correspond to this study. For NRIXS, hematite data are from Dauphas et

804 al. (2012) and goethite data are from this study. No NRIXS iron β-factor is published

805 yet for pyrite.

806

807 **Figure 8.** Temperature dependence of the oxygen α-factor between hematite and

808 goethite. For GGA and GGA+U, hematite data are from Blanchard et al. (2009) while

809 goethite data are from this study. Results of the semi-empirical approach of Zheng

810 (1991, 1998) are shown for comparison, as well as the following experimental data:

811 Exp. 1 corresponds to data from Bao and Koch (1999) where goethite was synthesized

812 at high pH (>14), and Exp. 2 combines the hematite-water isotopic fractionation

813 factors from Bao and Koch (1999) with goethite-water data at low pH (~1 to 2) from
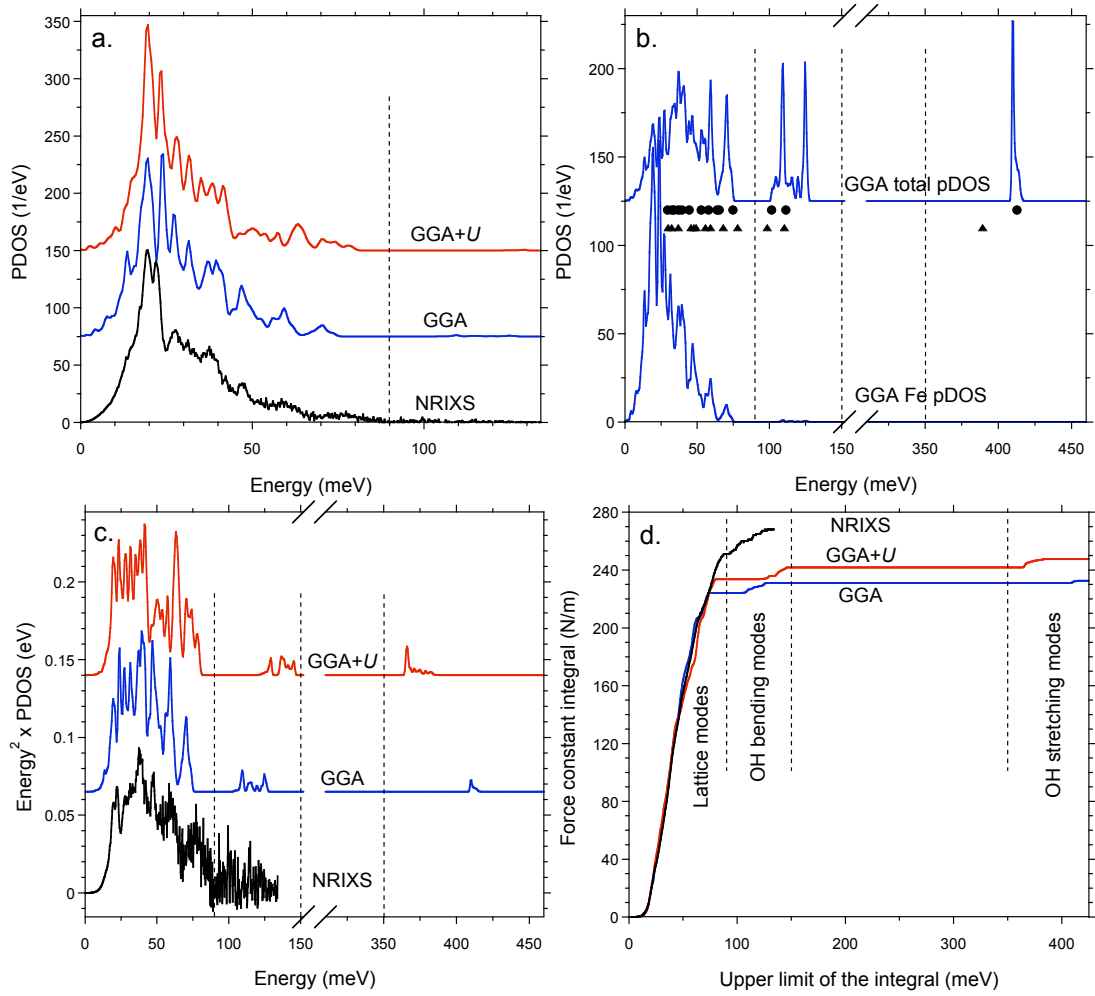
814 Yapp (2007).

815

815

Figure 1.
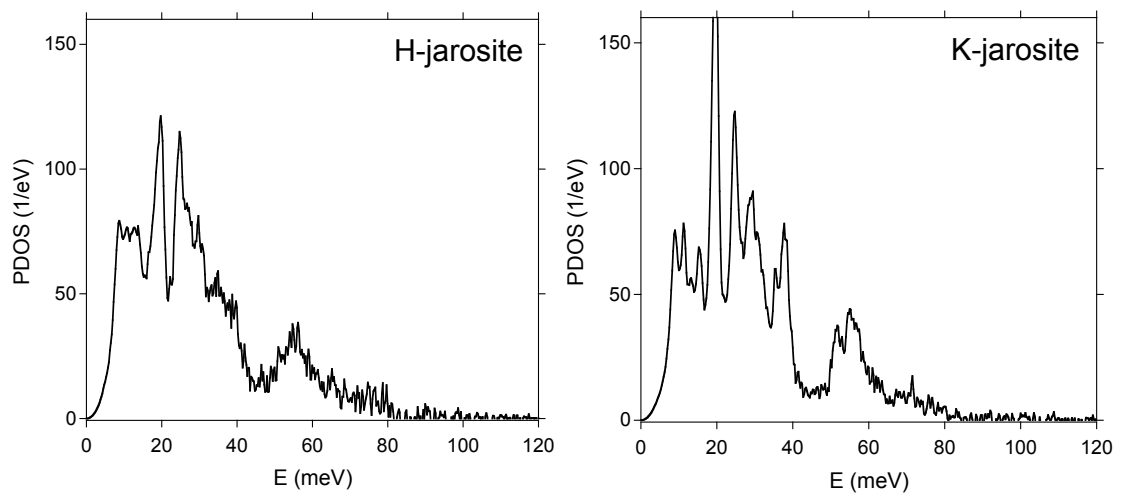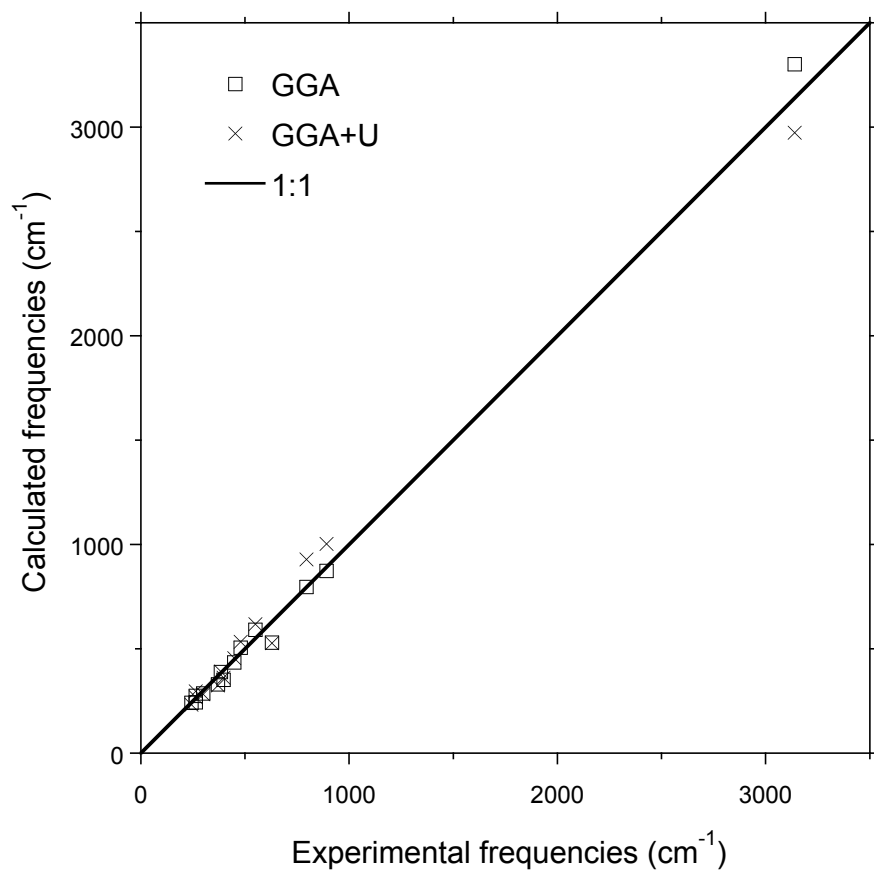
816

817

818

819
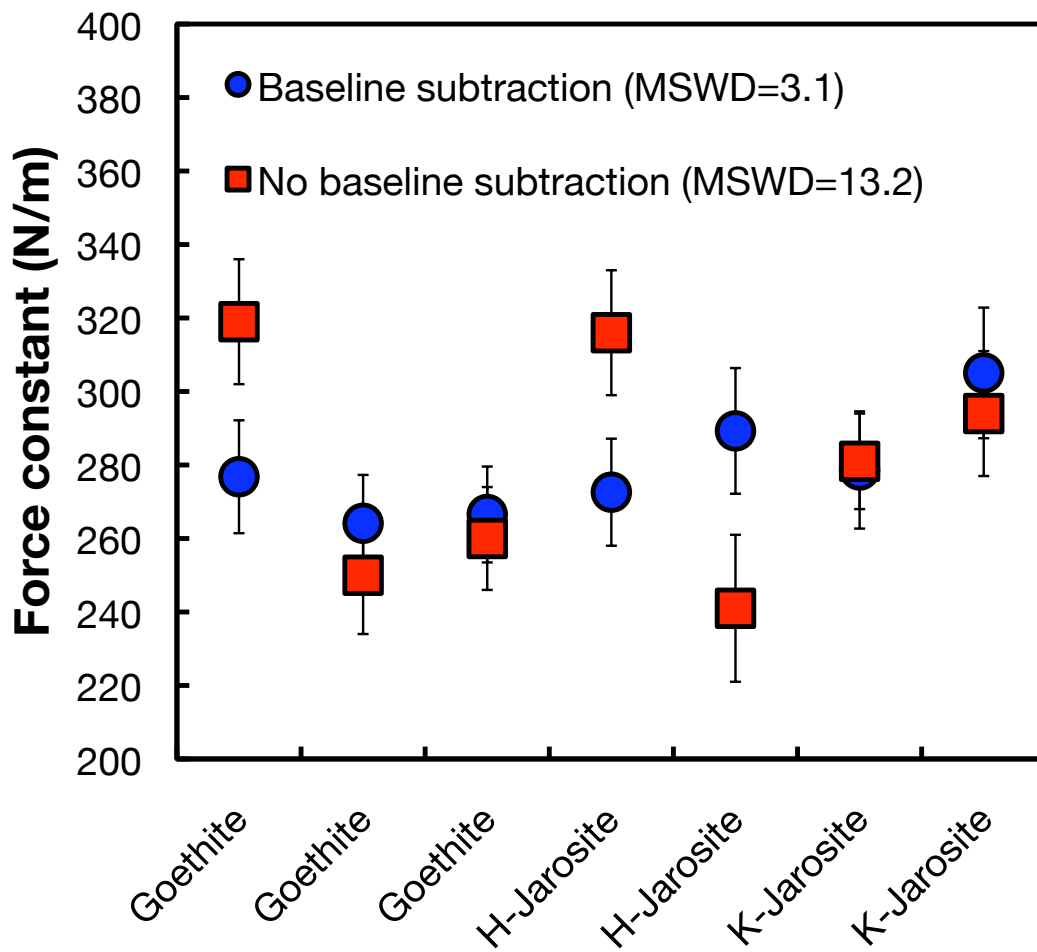
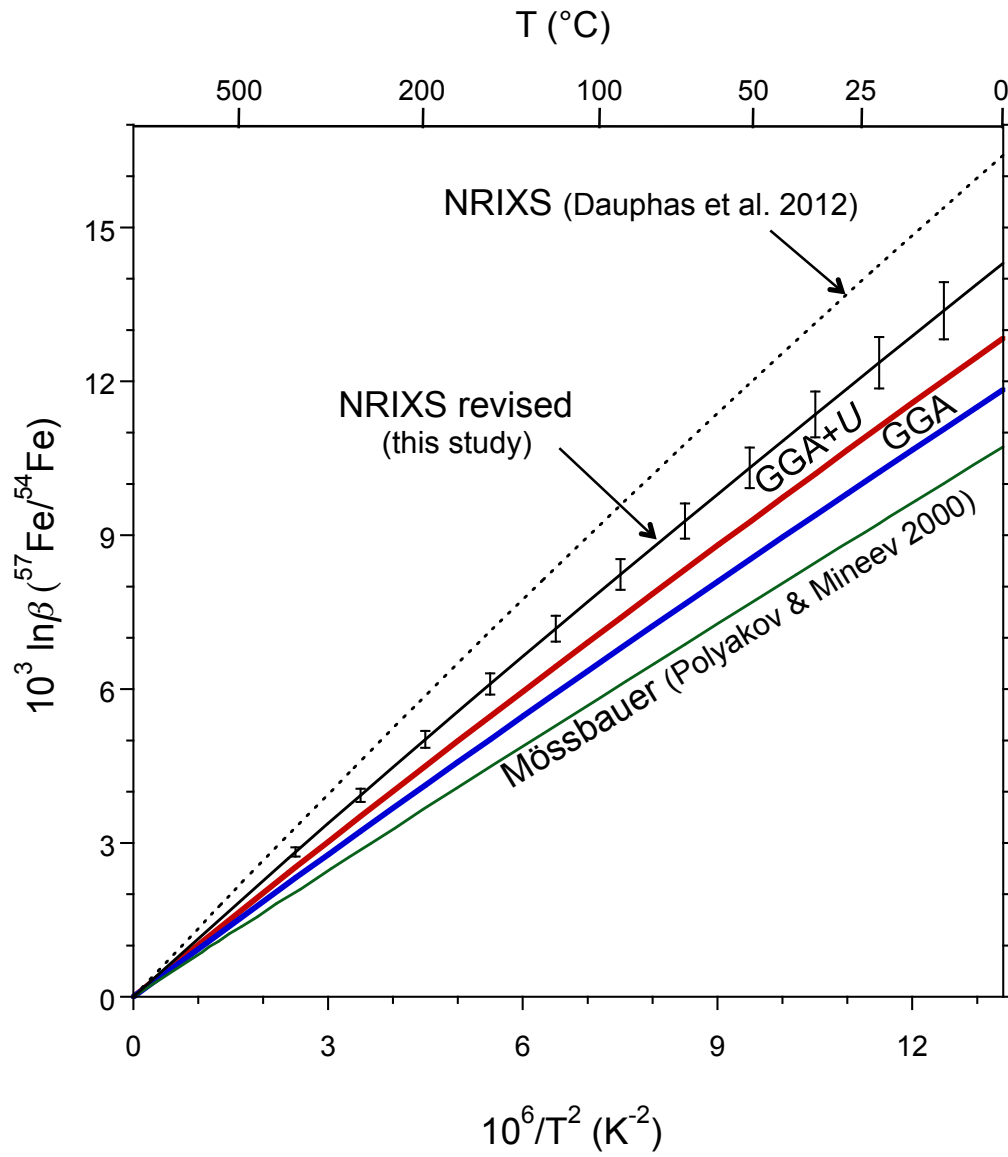820 **Figure 2.**

821

822

823

824 **Figure 3.**

825

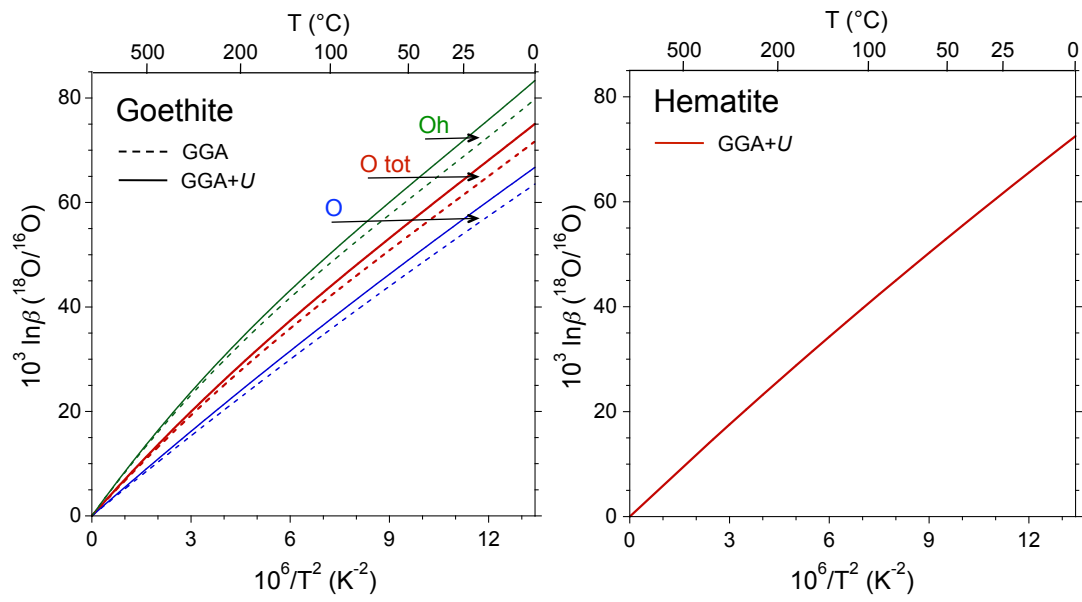826   **Figure 4.**

827

828

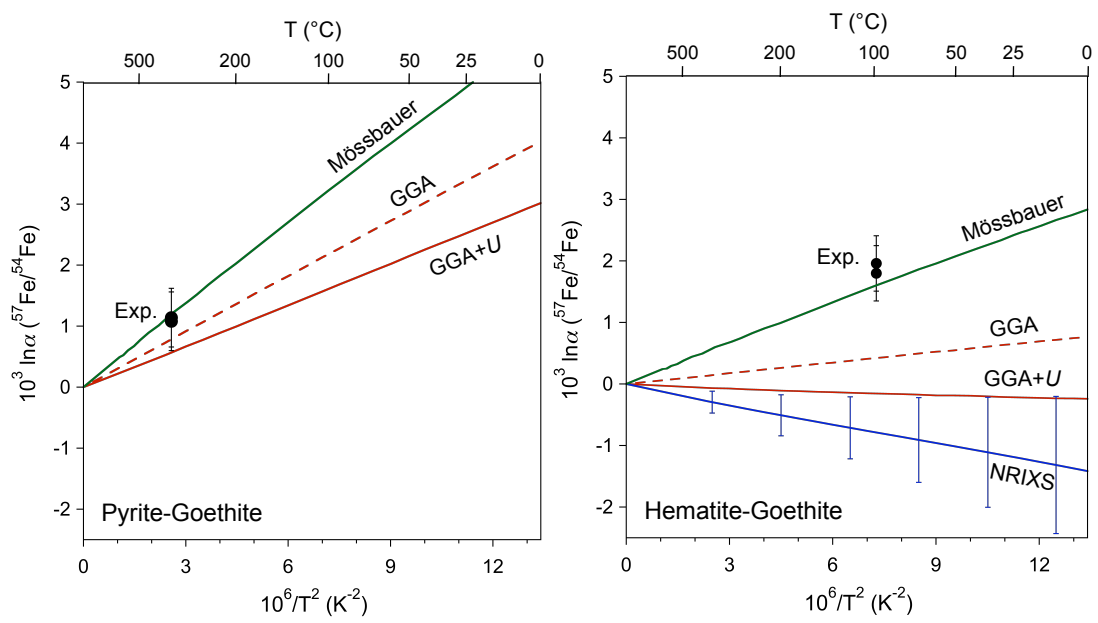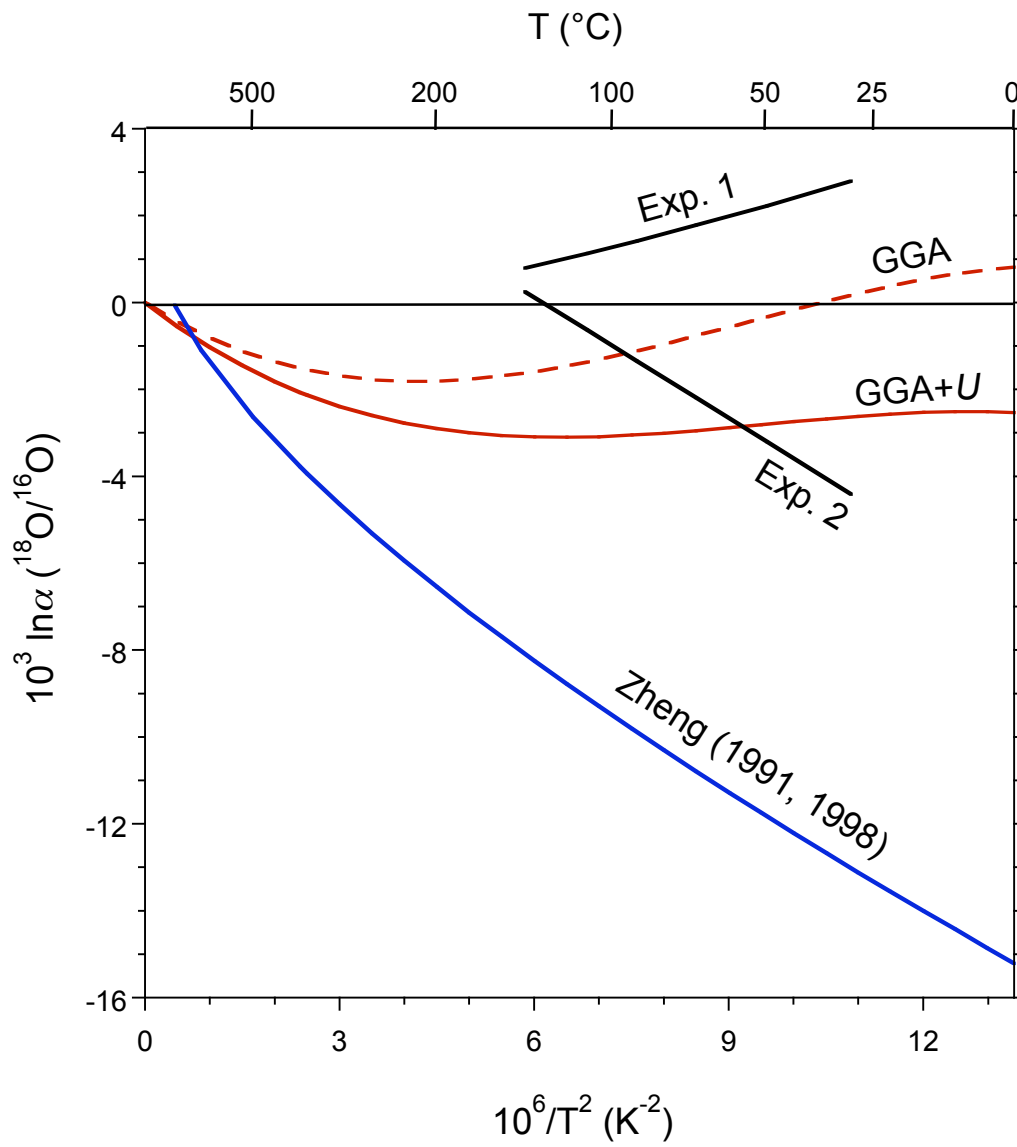829   **Figure 5.**

830

831

832

833

834 **Figure 6.**

835

836

837

838

839

840 **Figure 7.**

841

842

843   **Figure 8.**